



Title	Thickness dependence of proton conductivity of anodic ZrO ₂ -WO ₃ -SiO ₂ nanofilms
Author(s)	Ye, Ke; Aoki, Yoshitaka; Tsuji, Etsushi; Nagata, Shinji; Habazaki, Hiroki
Citation	Journal of Power Sources, 205, 194-200 https://doi.org/10.1016/j.jpowsour.2012.01.083
Issue Date	2012-05-01
Doc URL	http://hdl.handle.net/2115/49115
Type	article (author version)
File Information	JPS205_194-200.pdf



[Instructions for use](#)

Thickness Dependence of Proton Conductivity of Anodic ZrO₂-WO₃-SiO₂ Nanofilms

Ke Ye,^a Yoshitaka Aoki,^{a,b} Etsushi Tsuji,^{a,b} Shinji Nagata,^c and Hiroki
Habazaki^{a,b,*}

^a Graduate School of Chemical Sciences and Engineering; and ^b Faculty of
Engineering, Hokkaido University, Sapporo, Hokkaido, 060-8628, Japan

^c Institute for Materials Research, Tohoku University, Sendai 980-8577, Japan

Corresponding author: Phone/Fax: +81-11-706-6575, e-mail:

habazaki@eng.hokudai.ac.jp

Abstract: Amorphous $\text{ZrO}_2\text{-WO}_3\text{-SiO}_2$ nanofilms are simply prepared by anodizing of sputter-deposited $\text{Zr}_{37}\text{W}_{47}\text{Si}_{16}$ alloy at several formation voltages for 1.8 ks in 0.1 mol dm^{-3} phosphoric acid electrolyte at 20°C . Efficient proton conductivity was observed after thermal treatment at 250°C with the conductivity enhanced by reducing the film thickness. The conductivity is enhanced more than one order of magnitude by reducing the thickness from 300 to 140 nm. The anodic oxide films consist of two layers, comprising a thin outer ZrO_2 layer free from silicon and tungsten species and an inner main layer containing all zirconium, silicon and tungsten species. The thickness-dependent conductivity of the anodic $\text{ZrO}_2\text{-WO}_3\text{-SiO}_2$ films is associated with the conductivity of the outer ZrO_2 layer, which increases exponentially with reducing the film thickness. The area-specific resistivity of $0.14 \Omega \text{ cm}^2$, which is below the minimum requirement ($0.2 \Omega \text{ cm}^2$) for a practical electrolyte membrane in commercial fuel cells, is achieved at a temperature at 225°C for 100 nm-thick anodic $\text{ZrO}_2\text{-WO}_3\text{-SiO}_2$ films.

Keywords: amorphous materials; anodic oxidation; ion conducting materials; proton transport; nanofilms

1. Introduction

Anodizing of valve metals, including aluminum, titanium, zirconium, niobium, hafnium and tantalum, leads to formation of barrier-type (compact) or self-organized nanoporous anodic oxide films, depending on the electrolytes used. The oxide films formed are dielectrics or semiconductors with useful

properties that make them of great interest for many applications, including solid electrolytic capacitors, solar cells, photocatalysis, electrochromic devices, and self-cleaning materials [1–5].

It is known that anodic oxide films usually contain hydrogen species [6], and the authors recently reported that amorphous $\text{ZrO}_2\text{-WO}_3$ nanofilms, prepared by anodizing of $\text{Zr}_{50}\text{W}_{50}$ alloy in phosphoric acid electrolyte, revealed efficient proton conductivity even below 200°C [7]. $\text{ZrO}_2\text{-WO}_3$ is an attractive acid catalyst with its Brønsted acidity being comparable to fully anhydrous hydrofluoric acid [8]. As a consequence of its strong acidity, the anodic $\text{ZrO}_2\text{-WO}_3$ films may have exhibited the efficient proton conductivity. Such proton-conductive nanofilms are of great interest for application to an electrolyte membrane for intermediate-temperature fuel cells (ITFCs), operating between $100\text{-}400^\circ\text{C}$ [9]. The ITFCs have several advantages over polymer electrolyte fuel cells, which operates below 100°C , under fully hydrated conditions [10,11]. The fuel cell operation at intermediate temperatures allows the use of non-precious metal electrocatalysts [12] and a range of fuels including hydrocarbons [13] and facilitates simpler module designs compared with high-temperature solid oxide fuel cell. For the use of anodic $\text{ZrO}_2\text{-WO}_3$ films to fuel cell applications, a hydrogen membrane fuel cell (HMFC), proposed by Ito et al. [14], may be suitable. The HMFC consists of an ultrathin proton-conducting electrolyte membrane supported on a dense hydrogen-permeable membrane metal anode. This fuel cell has an advantage for the use of ultrathin electrolyte membrane, because the electrolyte membrane can be formed on the non-porous anode. Such cell can be formed by the complete

conversion of a Zr-W alloy thin film, deposited on the anode membrane by a PVD technique, to anodic $\text{ZrO}_2\text{-WO}_3$ by anodizing.

In addition to the efficient proton conductivity, the anodic $\text{ZrO}_2\text{-WO}_3$ films exhibited a unique thickness-dependent conductivity; the conductivity was enhanced more than one order of magnitude by reducing the film thickness to less than 120 nm. Thus, the proton conductivity of anodic $\text{ZrO}_2\text{-WO}_3$ films is of practical and fundamental interest. Although the efficient proton conductivity of the anodic $\text{ZrO}_2\text{-WO}_3$ films deteriorated thermally above 200°C, the authors recently reported that the thermal stability of the proton-conducting anodic $\text{ZrO}_2\text{-WO}_3$ nanofilms was significantly enhanced by the addition of SiO_2 species into anodic oxide films from alloy substrate, because of the suppression of the formation of a poorly conducting layer by inter-diffusion between the alloy substrate and the anodic film during post-annealing at elevated temperatures [15].

In the present study, the thickness dependence of the proton conductivity of the anodic $\text{ZrO}_2\text{-WO}_3\text{-SiO}_2$ films has been examined in detail. The conductivity is enhanced by reducing the thickness from 300 nm, with the significant change appearing between 200 and 300 nm. Such thickness-dependent conductivity has been discussed by measuring the conductivity of each layer of the anodic oxide films comprising a thin outer ZrO_2 layer free from silicon and tungsten species and an inner main layer containing all zirconium, silicon and tungsten species.

2. Experimental

The $Zr_{37}W_{47}Si_{16}$ alloy films, ~350 nm thick, were prepared by DC magnetron sputtering on to flat glass and aluminum substrates [15]. Prior to sputtering, the latter substrates were electropolished and subsequently anodized to provide a flat and smooth surface. The specimens prepared on aluminum substrates were used mostly for the characterization of the anodic oxide films by transmission electron microscope (TEM), Rutherford backscattering spectroscopy (RBS) and elastic recoil detection analysis (ERDA). The target used for the preparation of the alloy films was 99.9% zirconium disk of 100 mm in diameter with three 99.999 % silicon plates (16 × 16 mm) and five 99.99 % tungsten discs (20 mm in diameter) located symmetrically on the erosion region. The deposited films were anodized galvanostatically at a constant current of 10 A m⁻² up to selected voltages with current decay for 30 min in a stirred aqueous solution of 0.1 mol dm⁻³ phosphoric acid at 20°C to form anodic oxide films. A platinum sheet was used as a counter electrode. After anodizing, the specimens were washed carefully with Milli-Q water and then dried under warm air stream.

Ionic conductivity of anodic films was measured by AC impedance method. Au button electrodes (100 nm thick, 1 mm diameter) were deposited on the top of the anodic oxide films by ion etcher (Hitachi E1030) through a shadow mask to form a Zr-W-Si/anodic oxide/Au stack. The electrical lead of Au fine wire (0.05 mm Φ) was attached to the top and bottom electrodes by using Au paste (Nilaco). Then, all the specimens were post-annealed at 250°C in dry Ar atmosphere for 1.5 h. This post-annealing treatment was indispensable for activating the proton conductivity. Impedance spectroscopy measurements were carried out for the

stack by the frequency response analyzer (Solartron 1260) in a frequency range of 10 to 10^7 Hz at AC amplitude of 20 mV. All the measurements were carried out under dry and humidified atmospheres. The non-humidified, dry Ar atmosphere was controlled by flowing ultrapure Ar (99.9999%) gas at a rate of $80 \text{ cm}^3 \text{ min}^{-1}$. The humidified Ar atmosphere was prepared by bubbling the Ar gas at a rate of $80 \text{ cm}^3 \text{ min}^{-1}$ through pure H_2O at $30 \text{ }^\circ\text{C}$ ($p_{\text{H}_2\text{O}} = 0.041 \text{ atm}$). Deuterated Ar atmosphere was also prepared by bubbling the Ar gas at a rate of $80 \text{ cm}^3 \text{ min}^{-1}$ through pure D_2O at 32°C ($p_{\text{D}_2\text{O}} = 0.041 \text{ atm}$). For the isotope-effect study, the specimens were kept at 200°C for 24 h in the Ar/ H_2O or Ar/ D_2O atmosphere, prior to the conductivity measurements in the respective environments at several temperatures. The conductivity in dry Ar atmosphere was also measured for the specimens immersed in 0.1 mol dm^{-3} ammonium fluoride ethylene glycol solution to remove an outer ZrO_2 layer free from tungsten and silicon species in the anodic oxide films.

Elemental depth profiling analyses of the anodic oxide films were carried out by glow discharge optical emission spectroscopy (GDOES) using a Jobin-Yvon 5000 RF instrument in an Ar atmosphere of 600 Pa by applying RF of 13.56 MHz and power of 35 W. The wavelengths of 339.198, 429.461, 288.158, 121.567, 178.287 and 130.217 nm were used for the analysis of zirconium, tungsten, silicon, hydrogen, phosphorus and oxygen, respectively. The signals were detected from a circular area of approximately 4 mm diameter.

Vertical cross-sections of the anodic oxide films were observed using JEOL JEM-2000FX and JEM-2010 transmission electron microscopes (TEM)

operating at 200 kV. The ultrathin cross-sectional specimens were prepared by using ultramicrotomy (RMC, MT-7). The compositions of the anodic films and alloy films were determined by RBS, using a 2.0 MeV He^{2+} ion beam supplied by a tandem-type accelerator at Tohoku University. The scattered particles were detected at 170° to the incident beam direction, which was normal to the specimen surface. The data were analyzed using the RUMP program. In elastic recoil detection (ERD) analysis, the hydrogen in the samples, which are recoiled in the forward directions, were detected at 30° to the direction of a 2.8 MeV He^{2+} ion beam.

3. Results and Discussion

The anodic $\text{ZrO}_2\text{-WO}_3\text{-SiO}_2$ films were formed by anodizing of the sputter-deposited $\text{Zr}_{37}\text{W}_{47}\text{Si}_{16}$ alloy at several formation voltages between 25 V and 170 V in 0.1 mol dm^{-3} phosphoric acid electrolyte. The thicknesses of the anodic oxide films varied linearly with the anodizing voltage from 50 to 340 nm. Figure 1 shows the cross-sectional TEM images of the anodic films formed at 150 V and 50 V and post-annealed at 250°C . In every case, the anodic films annealed at 250°C consist of two layers (Figs. 1a and 1b), comprising a thin outer oxide layer and an inner oxide layer, which are developed on the alloy substrate. Fig. 1 also reveals a sharp interface between the oxide layer and alloy substrate with nm thickness precision. In Fig. 1a the thin outer layer, which occupies 9% of the overall thickness, reveals a diffraction contrast, indicating the presence of a nanocrystalline phase. In contrast, the inner layer is amorphous as suggested by

the absence of the diffraction contrast. The selected area electron diffraction (SAED) pattern of the outer layer is identical to a crystalline ZrO_2 phase and that of the inner oxide layer shows only diffuse rings, typical of amorphous material. Similar image and SAED patterns are obtained for the thin anodic film formed at 50 V (Fig. 1b), but the diffraction contrast in the outer layer is not obvious and only a faint diffraction spots are detected in SAED. Thus, the crystallization is more proceeding for the thicker anodic oxide film. The high resolution image of the outer layer of the 300 nm-thick anodic oxide films (Fig. 1c) reveals that nanocrystals of ZrO_2 with sizes of 10 nm or less are precipitated in an amorphous matrix. The crystalline oxide should be formed during annealing at 250°C, since the outer layer was amorphous under the as-anodized condition [7]. The inner amorphous oxide layer is $\text{ZrO}_2\text{-WO}_3\text{-SiO}_2$ mixed phase, while the outer layer is essentially free from tungsten and silicon species, as reported previously [15]. The formation of the thin outer ZrO_2 layer is associated with faster migration of Zr^{4+} ions, compared with the W^{6+} and Si^{4+} ions, during film growth under the high electric field. The detail of the film growth has been discussed in our previous paper [15]. In addition, phosphate anions are incorporated into the outer 50% of the film thickness, as clearly seen in later GDOES depth profiles.

As is well known, the thickness of anodic oxide films changes linearly with anodizing voltage. This is true for the present anodic oxide films. Table 1 shows the thicknesses of the outer and inner layers as well as total film thicknesses of the anodic oxide films formed at 25-170 V. The compositions of the outer and inner layers, determined by RBS, are independent of film thickness, being ZrO_2

and $(\text{Zr}_{0.31}\text{W}_{0.50}\text{Si}_{0.19})\text{O}_{2.50}$, respectively, as reported in our previous report [15]. The incorporated phosphorus species were neglected in the quantitative RBS analysis, due to low sensitivity, but in accord with previous studies [16-17], the phosphorus content in anodic oxide films formed on valve metals in phosphoric acid is usually a few atomic percent. Thus, the similar phosphorus content is presumed also in the present anodic oxide films. The influence of the presence of phosphate in the anodic films on the proton conductivity is the subject of future study, although negligible influence of phosphate on the proton conductivity of the anodic $\text{ZrO}_2\text{-WO}_3$ films free from silion species has been reported [7].

After depositing an Au button electrode on the anodic oxide films, the resistivity across the anodic films was determined by AC impedance spectroscopy. Efficient proton conductivity occurred in the films after thermal treatment at 250°C in dry and humidified atmospheres, even though the films without thermal treatment were poorly-conductive [15]. Thus, in the present study the conductivity measurements were carried out after activation treatment at 250°C in a dry argon atmosphere for 1.5 h. Nyquist plots reported in our previous study [15] of the heated specimens revealed a small semicircle in the high-frequency region and a spike in the low frequency region, typical of ionic conductors with blocking electrodes [18]. The high-frequency semicircle must be associated with ionic conduction in the oxide film and become smaller with increasing the measuring temperature. The stable proton conductivity was observed even in dry atmosphere, due to the presence of native proton in the anodic oxide films. The low-frequency spike was related to charge buildup at the

film/electrode interface. The presence of the spike also indicated negligible contribution of electronic conductivity in the anodic oxide films.

The Arrhenius plots of the proton conductivity, σ , of the anodic oxide films with various thicknesses in a dry Ar atmosphere are shown in Figure 2a. All films exhibit linear temperature dependence in the measured temperature range. Interestingly, the σ value of the anodic $\text{ZrO}_2\text{-WO}_3\text{-SiO}_2$ films is remarkably increased by reducing film thickness, d , to less than 300 nm. Furthermore, the activation energy, E_a , of proton conductivity also varies with d . In case of $d > 300$ nm, the E_a value is $59.0 \pm 1.2 \text{ kJ mol}^{-1}$, which decreases to $52.0 \pm 0.7 \text{ kJ mol}^{-1}$ at $d < 220$ nm. The 100 nm-thick anodic $\text{ZrO}_2\text{-WO}_3\text{-SiO}_2$ film shows the area-specific resistivity of $0.14 \text{ } \Omega \text{ cm}^2$, which is below the minimum requirement ($0.2 \text{ } \Omega \text{ cm}^2$) [19] for a practical electrolyte membrane in commercial fuel cells, at 225°C .

Figure 2b shows thickness dependence of σ of the anodic $\text{ZrO}_2\text{-WO}_3\text{-SiO}_2$ films on $\text{Zr}_{37}\text{W}_{47}\text{Si}_{16}$, measured at 100°C in dry Ar. The thickness dependence of the silicon-free anodic $\text{ZrO}_2\text{-WO}_3$ films on the $\text{Zr}_{50}\text{W}_{50}$ [7] is also shown for comparison. The σ values of the anodic $\text{ZrO}_2\text{-WO}_3\text{-SiO}_2$ films are apparently constant at and above 300 nm, but increase with reducing the film thickness, particularly between 200 and 300 nm. The σ value of the 200 nm-thick film is more than 10 times that of the 300 nm-thick film. This thickness dependency of the $\text{ZrO}_2\text{-WO}_3\text{-SiO}_2$ films is quite different from that of the silicon-free films. The anodic $\text{ZrO}_2\text{-WO}_3$ films also reveal the large thickness-dependent proton conductivity, but a notable conductivity increase by more than one order of magnitude appears below 120 nm, as seen in Figure 2b. Although the thickness

range showing the marked conductivity enhancement is different for the anodic films with and without silicon species, the conductivities of both anodic films are similar in the thickness range between 120 and 200 nm. The detail mechanism for the thickness dependency will be discussed later.

In order to confirm that the conducting ionic species in the present anodic $\text{ZrO}_2\text{-WO}_3\text{-SiO}_2$ films are proton, the H/D isotope effect on conductivity was examined. Proton conductivity as a function of temperature was measured in argon atmospheres containing H_2O or D_2O for the film with 200 nm thickness (Figure 3). The anodic film shows the clear H/D effect [20,21] on proton conductivity in the measured temperature range and the σ value in $\text{Ar/D}_2\text{O}$ (σ_{D}) is lower than that in $\text{Ar/H}_2\text{O}$ (σ_{H}) by a factor of $\sigma_{\text{H}}/\sigma_{\text{D}} = 1.26 \pm 0.05$. The activation energy of σ_{D} is very similar to that of σ_{H} . Although the ratio of $\sigma_{\text{H}}/\sigma_{\text{D}}$ is slightly smaller than the value expected for classical proton-hopping migration (ca. 1.4) [22], a proton can be assigned to the main charge carriers in the anodic $\text{ZrO}_2\text{-WO}_3\text{-SiO}_2$ film. A nonclassical isotope effect of the anodic film might indicate that the rate-determining step of proton hopping is the dissociation of hydrogen bond between the protonic carrier and coordinated oxygen as is the case with intermediate-temperature proton conductors like SnP_2O_7 and high-temperature perovskite oxides [22,23]. Similar H/D isotope effect was obtained for the present anodic films with different thicknesses.

As shown above, the anodic oxide films on the $\text{Zr}_{37}\text{W}_{47}\text{Si}_{16}$ consist of two layers: an outer ZrO_2 layer and an inner layer containing all alloy-constituting element species. The each layer might have different proton conductivity. To

examine the proton conductivity of the outer and inner layers separately, the outer thin ZrO₂ layer was removed by chemical sectioning in ethylene glycol solution containing 0.1 mol dm⁻³ ammonium fluoride. The chemical sectioning of the outer ZrO₂ layer was monitored by GDOES depth profile analysis. Figure 4a reveals the depth profile of the anodic film of 300 nm thickness before chemical sectioning. Obviously, outer layer is free from tungsten and silicon species, and the inner layer contains all zirconium, tungsten and silicon species. Phosphorus species, incorporated from phosphoric acid electrolyte, distribute to the depth of approximately 40% of the inner layer. Peaks of zirconium, tungsten and phosphorus intensities at the boundary between the inner and outer layers may be artifact, because the enrichment of these species at this boundary region was not detected by RBS analysis. The ratio of the sputtering time for the outer layer to that for the inner layer is not consistent with their thickness ratio (Table 1), indicating slower sputtering in the outer layer in comparison with the inner layer during depth profile analysis. Hydrogen species are also present in the anodic film with the concentration being higher in the outer layer in comparison with the inner layer. The hydrogen concentration in the inner layer decreases slightly with increasing a depth, with negligible influence of phosphate incorporation on the hydrogen profile. The depth profile of the specimen after chemical sectioning for 54 h (Figure 4b) discloses the thinning of the outer layer with the inner layer remaining unchanged, suggesting uniform thinning of the anodic film from the film surface. After chemical sectioning for 108 h, the outer ZrO₂ layer is absent, and the sputtering time and elemental profile for the inner layer are still

unchanged. Thus, only the inner layer is remained without damaging in the solution.

After removing the outer ZrO_2 layer from the anodic films formed at several anodizing voltages, proton conductivity was measured and compared with that before removing the outer layer. The results are shown in Figure 5. The removal of the 27 nm-thick outer layer from the 300 nm-thick anodic film increases largely the σ value and change the E_a value from 59.0 to 48.0 kJ mol^{-1} (Fig. 5a). The conductivity is enhanced by a factor of more than 10 at and below 100°C. With reducing the film thickness of the anodic oxide films, the conductivity enhancement by removing the outer layer becomes less significant (Fig. 5), and the σ value of the 50 nm-thick anodic oxide film is almost unchanged even after removing the 4.5 nm-thick outer layer. The results shown in Figure 5 indicates that the proton conductivity of the layered anodic films is predominantly controlled by the outer layer for the thick anodic films of ~300 nm thickness, while the inner layer determines the overall conductivity for this anodic films of less than 100 nm thickness.

Such change is associated with the thickness-dependent conductivity of the outer layer. The conductivity of the outer ZrO_2 layer was estimated from the change in the conductivity by removing the outer layer, and the σ values of the outer and inner layers at 100°C as a function of film thickness are plotted in Figure 6. Similar trend was observed at different temperatures. It is remarkable that the σ value of the inner layer is little dependent upon the thickness. In contrast, the σ value of outer ZrO_2 layer is exponentially increased with reducing

its thickness. The log-log plot of σ vs thickness of the outer ZrO_2 layer is almost linear with a slope of 2.6 ± 0.7 (Fig. 6b). The activation energy E_a increases linearly with increasing the film thickness before removing the outer ZrO_2 layer, but its thickness dependence is also highly reduced after removing the outer layer (Fig. 6c). In case of the 50 nm-thick anodic oxide film, the E_a ($44.0 \pm 2.0 \text{ kJ mol}^{-1}$) before removing 4.5 nm-thick ZrO_2 layer is almost the same as that after removing the outer layer ($43.0 \pm 1.8 \text{ kJ mol}^{-1}$). However, the E_a is largely reduced from $59.0 \pm 1.2 \text{ kJ mol}^{-1}$ to $48.0 \pm 1.3 \text{ kJ mol}^{-1}$ by removing the ZrO_2 layer in case of 300 nm-thick anodic films (Fig. 6c). These results clearly indicate that the conductivity of the outer ZrO_2 layer is rate limiting when its thickness is $\sim 300 \text{ nm}$, but the contribution of the inner layer becomes important when the thickness of the anodic films is less than 100 nm. It should be also worth mentioning that even after removing the outer layer the H/D isotope effect on the proton conductivity, similar to Fig. 3, was observed.

Kim et al. reported that nanocrystalline yttria-stabilized ZrO_2 exhibits the proton conductivity of the order of $10^{-9} \text{ S cm}^{-1}$ at temperatures below 200°C , because proton given by the adsorbed water at external and internal surfaces can migrate through the grain boundary [24-26]. The conductivity reported by Kim et al. is lower than that of the outer ZrO_2 layer in the present study. Further, it is likely from Fig. 1 that nanocrystals of ZrO_2 are present at higher density in the thicker outer layers, while the conductivity is reduced by thickening of the outer layer. Thus, the grain boundaries along the ZrO_2 nanocrystals in the outer layer may not be a predominant diffusing path of proton.

The conductivity of the outer layer increases exponentially as a function of thickness in the measured thickness range (Fig. 6). This feature is very similar to the size-scaling of ionic conductivity found in the ion-conducting amorphous silicate thin films [20]. This size-scaling behavior is characteristic of amorphous nanofilms consisting of the highly-conducting pathway and poorly-conducting matrix with the concentration of the path below the percolation threshold.

Figure 7 shows the depth distribution of protons, determined by ERD analysis, in the anodic $\text{ZrO}_2\text{-WO}_3\text{-SiO}_2$ films with different thicknesses. Obviously, the outer part of the anodic oxide films contains relatively high concentration of protons with its concentration increasing with reducing the film thickness. Since the proton concentration in the anodic oxide film after post-annealing at 250°C was similar to that before annealing, the proton concentration was controlled by the anodizing voltage. Dehydration in the outer layer may proceed with increasing the anodizing voltage. Hydration-induced marked enhancement of proton conductivity has been reported for the amorphous zirconium phosphate nanofilms prepared by multiple spin casting [27]. Thus, it is also probable that dehydration during anodizing to higher voltages contributes to the reduced proton conductivity of the present anodic oxide films. In other words, the hydrated amorphous ZrO_2 outer layer shows relatively high proton conductivity. The outer layer contains phosphate derived from the electrolyte. The incorporation of phosphate may not affect largely the conductivity, because of the similar conductivity of the silicon-free anodic $\text{ZrO}_2\text{-WO}_3$ films with and without phosphate

[7]. Both the silicon-free and silicon-containing anodic films have the same outer ZrO_2 layer free from tungsten and silicon species.

Although the concentration of protons changes with the thickness of the anodic $\text{ZrO}_2\text{-WO}_3\text{-SiO}_2$ films, thermal treatment did not change the proton concentration. Thus, the activation of proton conductivity by the thermal treatment is not associated with the proton concentration. Even after removing the outer ZrO_2 layer, the thermal treatment was indispensable to activate the proton conductivity of the present anodic oxide films. Further structural characterization of the inner amorphous layer as well as evaluation of acidity of the oxide nanofilms is needed for understanding the activation mechanism of the proton conductivity.

4. Conclusions

In summary, the present work demonstrates that the anodic $\text{ZrO}_2\text{-WO}_3\text{-SiO}_2$ films show efficient proton conductivity below 250°C , and the ASR value of $0.14 \Omega \text{ cm}^2$, which is below the minimum requirement ($0.2 \Omega \text{ cm}^2$) for a practical electrolyte membrane in commercial fuel cells, is achieved at a temperature of 225°C for the 100 nm-thick anodic oxide film. The conductivity of the anodic oxide films is strongly dependent upon film thickness, due to thickness-dependent conductivity of the outer ZrO_2 layer of the anodic oxide films. Removal of the relatively thick ZrO_2 layer drastically increases the conductivity by more than one order of magnitude. The anodic $\text{ZrO}_2\text{-WO}_3\text{-SiO}_2$ films showing such

unique proton conducting behavior are promising as electrolyte membrane for fuel cells operating at intermediate temperatures.

Acknowledgement

The present work was supported in part by the Global COE Program (Project No. B01: Catalysis as the Basis for Innovation in Materials Science) from the Ministry of Education, Culture, Sports, Science and Technology, Japan, a Grant-in-Aid for Exploratory Research, No. 23656441 from the Japan Society for the Promotion of Science, and the Asahi Glass Foundation.

References

- [1] K. Shimizu, K. Kobayashi, G.E. Thompson, P. Skeldon, G.C. Wood, *Philos. Mag. B* 73 (1996) 461-485.
- [2] K. Tsujii, T. Yamamoto, T. Onda, S. Shibuichi, *Angew. Chem.* 109 (1997) 1042-1044; *Angew. Chem. Int. Ed. Engl.* 36 (1997) 1011-1012.
- [3] H. Habazaki, K. Shimizu, S. Nagata, K. Asami, K. Takayama, Y. Oda, P. Skeldon, G.E. Thompson, *Thin Solid Films* 479 (2005) 144-151.
- [4] E. Balaur, J.M. Macak, L. Taveira, P. Schmuki, *Electrochem. Commun.* 7 (2005) 1066-1070.
- [5] C.A. Grimes, *J. Mater. Chem.* 17 (2007) 1451-1457.

- [6] L. Iglesias-Rubianes, P. Skeldon, G.E. Thompson, U. Kreissig, D. Grambole, H. Habazaki, K. Shimizu, *Thin Solid Films* 424 (2003) 201-207.
- [7] D. Kowalski, Y. Aoki, H. Habazaki, *Angew. Chem. Int. Ed.* 48 (2009) 7582-7585.
- [8] G. Busca, *Chem. Rev.* 107 (2007) 5366-5410.
- [9] T. Norby, *Solid State Ionics* 125 (1999) 1-11.
- [10] K. Schmidt-Rohr, Q. Chen, *Nat. Mater.* 7 (2008) 75-83.
- [11] O. Diat, G. Gebel, *Nat. Mater.* 7 (2008) 13-14.
- [12] P. Heo, M. Nagao, M. Sano, T. Hibino, *J. Electrochem. Soc.* 154 (2007) B53-B56.
- [13] P. Heo, K. Ito, A. Tomita, T. Hibino, *Angew. Chem.* 120 (2008) 7959-7962; *Angew. Chem. Int. Ed.* 47 (2008) 7841-7844.
- [14] N. Ito, M. Iijima, K. Kimura, S. Iguchi, *J. Power Sources* 152 (2005) 200-203.
- [15] K. Ye, Y. Aoki, E. Tsuji, S. Nagata, H. Habazaki, *J. Electrochem. Soc.* 158 (2011) C385-C390.
- [16] Q. Lu, S. Mato, P. Skeldon, G.E. Thompson, D. Masheder, H. Habazaki, K. Shimizu, *Electrochim. Acta* 47 (2002) 2761-2767.
- [17] F. Le Coz, L. Arurault, S. Fontorbes, V. Vilar, L. Datas, P. Winterton, *Surf. Interface Anal.* 42 (2010) 227-233.
- [18] J.T.S. Irvine, D.C. Sinclair, A.R. West, *Adv. Mater.* 2 (1990) 132-138.
- [19] B.C.H. Steele, A. Heinzl, *Nature* 414 (2001) 345-352.
- [20] Y. Aoki, H. Habazaki, S. Nagata, A. Nakao, T. Kunitake, S. Yamaguchi, *J. Am. Chem. Soc.* 133 (2011) 3471-3479.

- [21] A.S. Nowick, A.V. Vaysleyb, *Solid State Ionics* 97 (1997) 17-26.
- [22] N. Bonanos, *Solid State Ionics* 53 (1992) 967-974.
- [23] M. Nagao, T. Kamiya, P. Heo, A. Tomita, T. Hibino, M. Sano, *J. Electrochem. Soc.* 153 (2006) A1604-A1609.
- [24] H.J. Avila-Paredes, E. Barrera-Calva, H.U. Anderson, R.A.D. Souza, M. Martin, Z.A. Munir, S. Kim, *J. Mater. Chem.* 20 (2010) 6235-6238.
- [25] S. Kim, H.J. Avila-Paredes, S. Wang, C.T. Chen, R.A.D. Souza, M. Martin, Z.A. Munir, *Phys. Chem. Chem. Phys.* 11 (2009) 3035-3038.
- [26] S. Kim, U. Anselmi-Tamburini, H.J. Park, M. Martin, Z.A. Munir, *Adv. Mater.* 20 (2008) 556-559.
- [27] Y. Aoki, K. Ogawa, H. Habazaki, T. Kunitake, Y.Z. Li, S. Nagata, S. Yamaguchi, *Chem. Mater.* 22 (2010) 5528-5536.

Figure captions

Figure 1. Transmission electron micrographs of an ultramicrotomed sections of the sputter-deposited $Zr_{37}W_{47}Si_{16}$ alloy film anodized at 150 V (a) and 50 V (b) for 1.8 ks in 0.1 mol dm^{-3} phosphoric acid electrolyte at $20 \text{ }^{\circ}\text{C}$ and then post-annealed at 250°C in dry Ar atmosphere for 1.5 h. (c) the high resolution image of the outer layer in (a).

Figure 2. a) Arrhenius plots and (b) thickness dependence of the proton conductivity, σ , across the anodic film measured in dry Ar atmosphere for the specimens formed by anodizing of the sputter-deposited $Zr_{37}W_{47}Si_{16}$ alloy at several voltages for 1.8 ks in 0.1 mol dm^{-3} phosphoric acid electrolyte at $20 \text{ }^{\circ}\text{C}$ and then post-annealed at 250°C in dry Ar atmosphere for 1.5 h. Thickness-dependence of the conductivity of the anodic ZrO_2 - WO_3 films free from silicon species [7] is also shown for comparison.

Figure 3. Arrhenius plots of the proton conductivity, σ , across the anodic film measured in Ar/ H_2O or Ar/ D_2O atmospheres ($p_{H_2O}=p_{D_2O}=0.041 \text{ atm}$) for the specimens formed by anodizing of the sputter-deposited $Zr_{37}W_{47}Si_{16}$ alloy at 100 V for 1.8 ks in 0.1 mol dm^{-3} phosphoric acid electrolyte at $20 \text{ }^{\circ}\text{C}$ and then post-annealed at 250°C in dry Ar atmosphere for 1.5 h.

Figure 4. GDOES depth profiles of the anodic ZrO_2 - WO_3 - SiO_2 films formed by anodizing at 150 V and immersed in 0.1 mol dm^{-3} ammonium fluoride ethylene glycol solution for different times t . a) $t = 0 \text{ h}$; b) $t = 54 \text{ h}$; c) $t = 108 \text{ h}$.

Figure 5. Arrhenius plot of the proton conductivity in dry Ar atmosphere for a) 300 nm-thick, b) 200 nm-thick, c) 100 nm-thick and d) 50 nm-thick $\text{ZrO}_2\text{-WO}_3\text{-SiO}_2$ anodic oxide films before and after dissolution of outer ZrO_2 layer in 0.1 mol dm^{-3} ammonium fluoride ethylene glycol solution.

Figure 6. a) Proton conductivity, σ in dry Ar atmosphere at $100 \text{ }^\circ\text{C}$ of the outer ZrO_2 layer (■) and the inner oxide layer (▲), as calculated from σ of the anodic films before and after removing outer ZrO_2 layer. b) The log-log plot of σ of the outer ZrO_2 layer (■). c) Thickness dependence of the activation energy E_a of the proton conductivity in dry Ar atmosphere of the films before and after removing the outer ZrO_2 layer.

Figure 7. Depth profiles of proton, determined by ERD analysis, for the sputter-deposited $\text{Zr}_{37}\text{W}_{47}\text{Si}_{16}$ alloy anodized at 50, 100 and 150 V for 1.8 ks in 0.1 mol dm^{-3} phosphoric acid electrolyte at $20 \text{ }^\circ\text{C}$ and then post-annealed at 250°C in dry Ar atmosphere for 1.5 h.

Table 1. Thicknesses of the individual layers of anodic oxide films formed on the sputter-deposited $Zr_{37}W_{47}Si_{16}$ alloy by anodizing at several voltages for 1.8 ks in 0.1 mol dm^{-3} phosphoric acid at 20°C and post-annealed at 250°C for 1.5 h.

Anodizing voltage, E [V]*	Total thickness, d [nm]	Thickness of the inner ZrO_2 - WO_3 - SiO_2 layer, d_1 [nm]	Thickness of the outer ZrO_2 layer, d_2 [nm]
25	50	45.5	4.5
50	100	91	9
70	140	127	13
90	180	164	16
100	200	182	18
110	220	200	20
130	260	237	23
150	300	273	27
170	340	309	31

*The thicknesses for the specimens anodized at 50, 100 and 150 V were determined by TEM observations and the others were estimated from their linear correlation between anodizing voltage and film thickness.

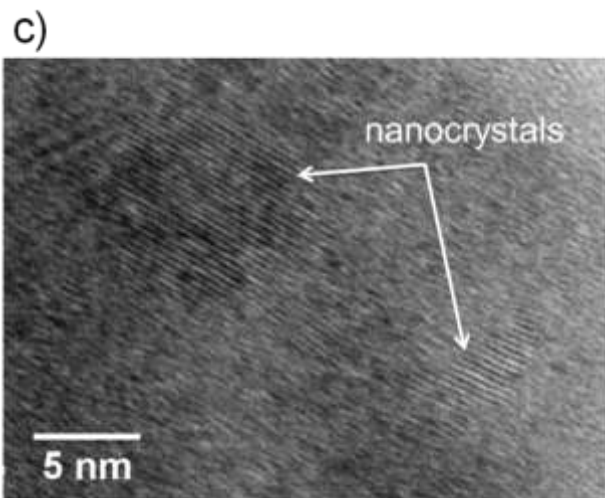
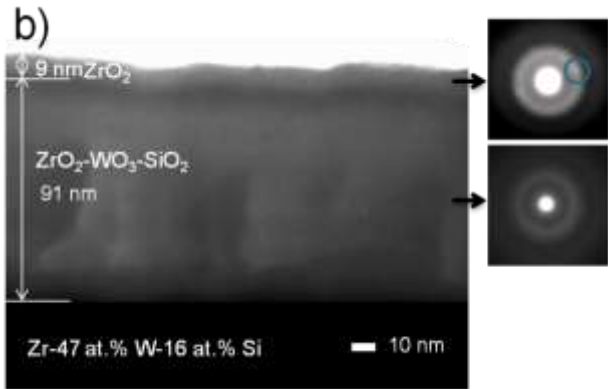
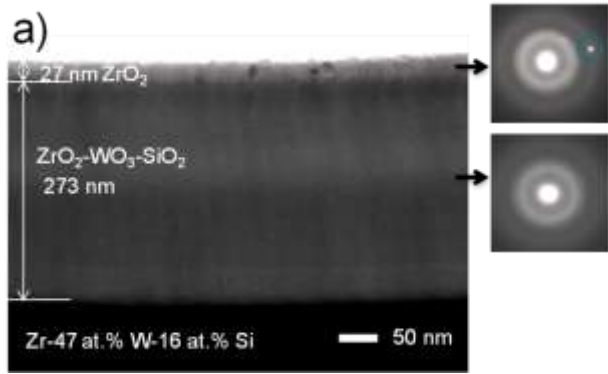


Figure 1.

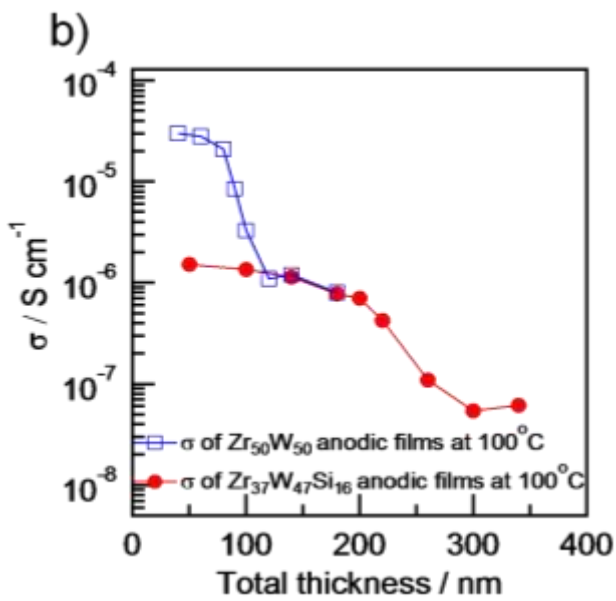
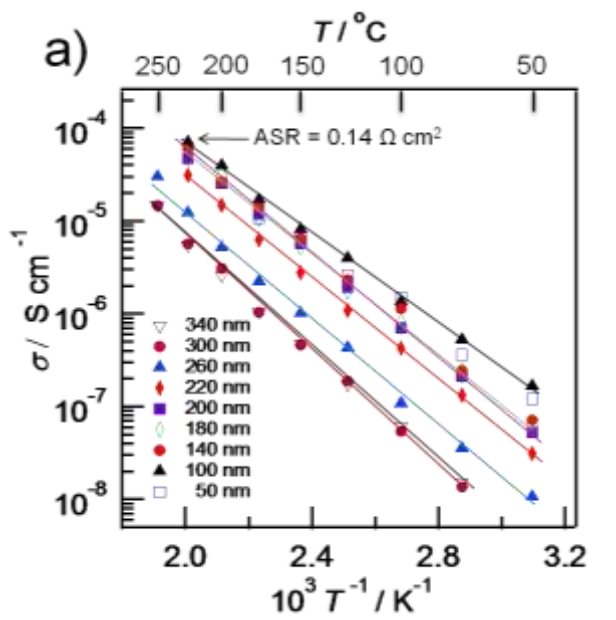


Figure 2.

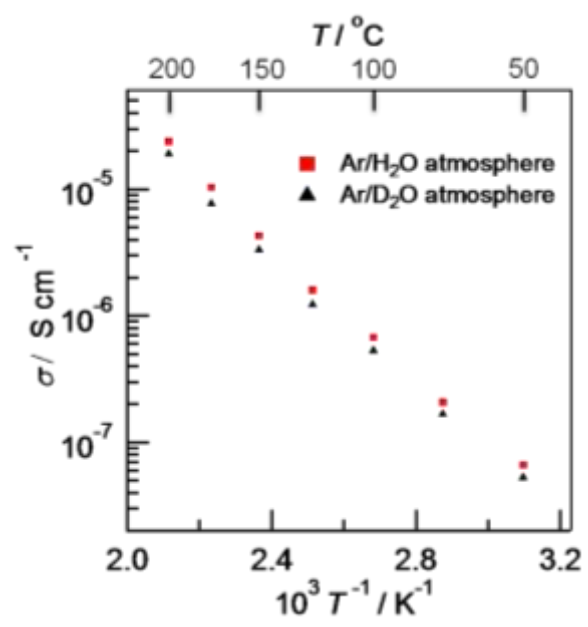


Figure 3.

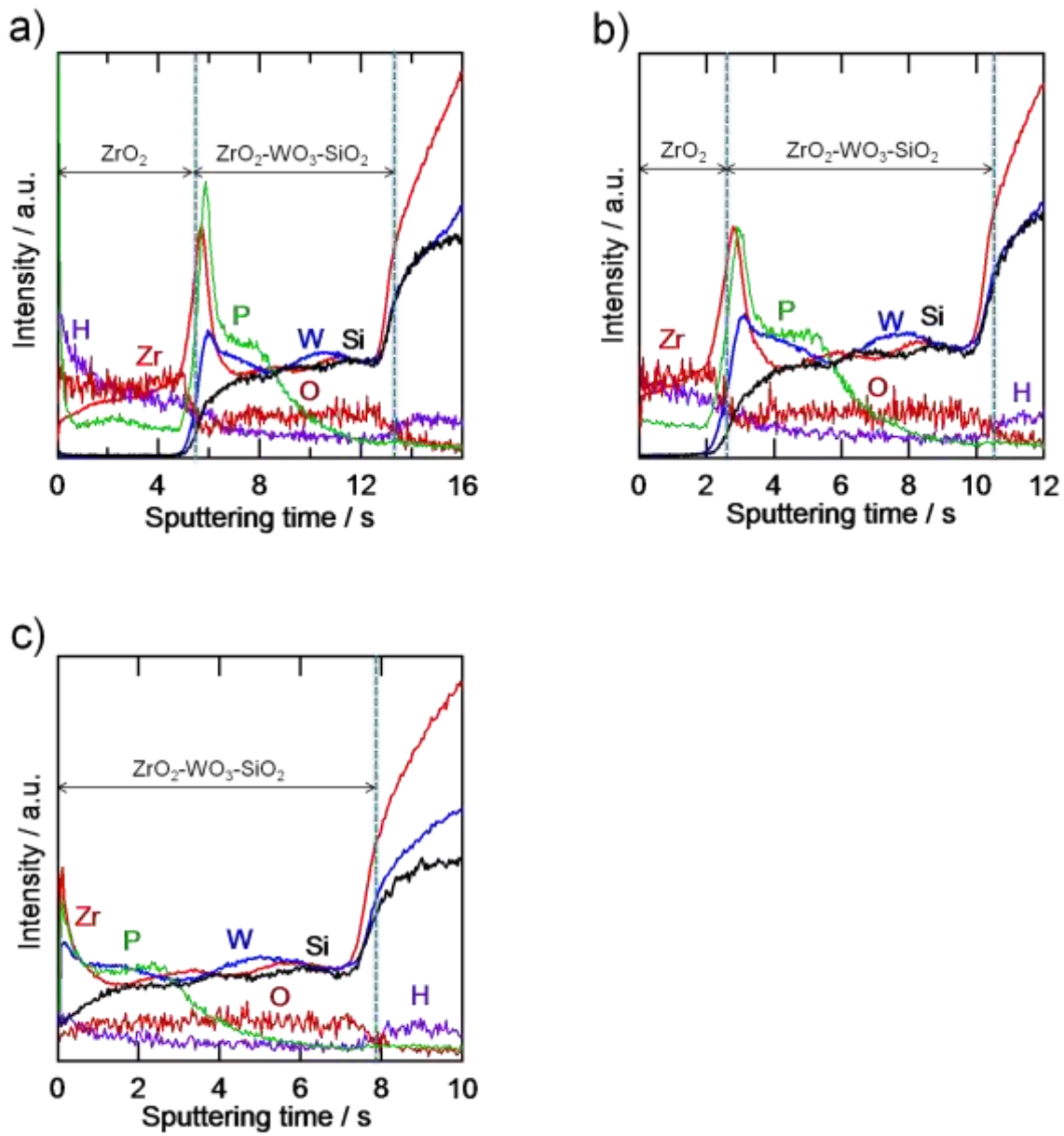


Figure 4.

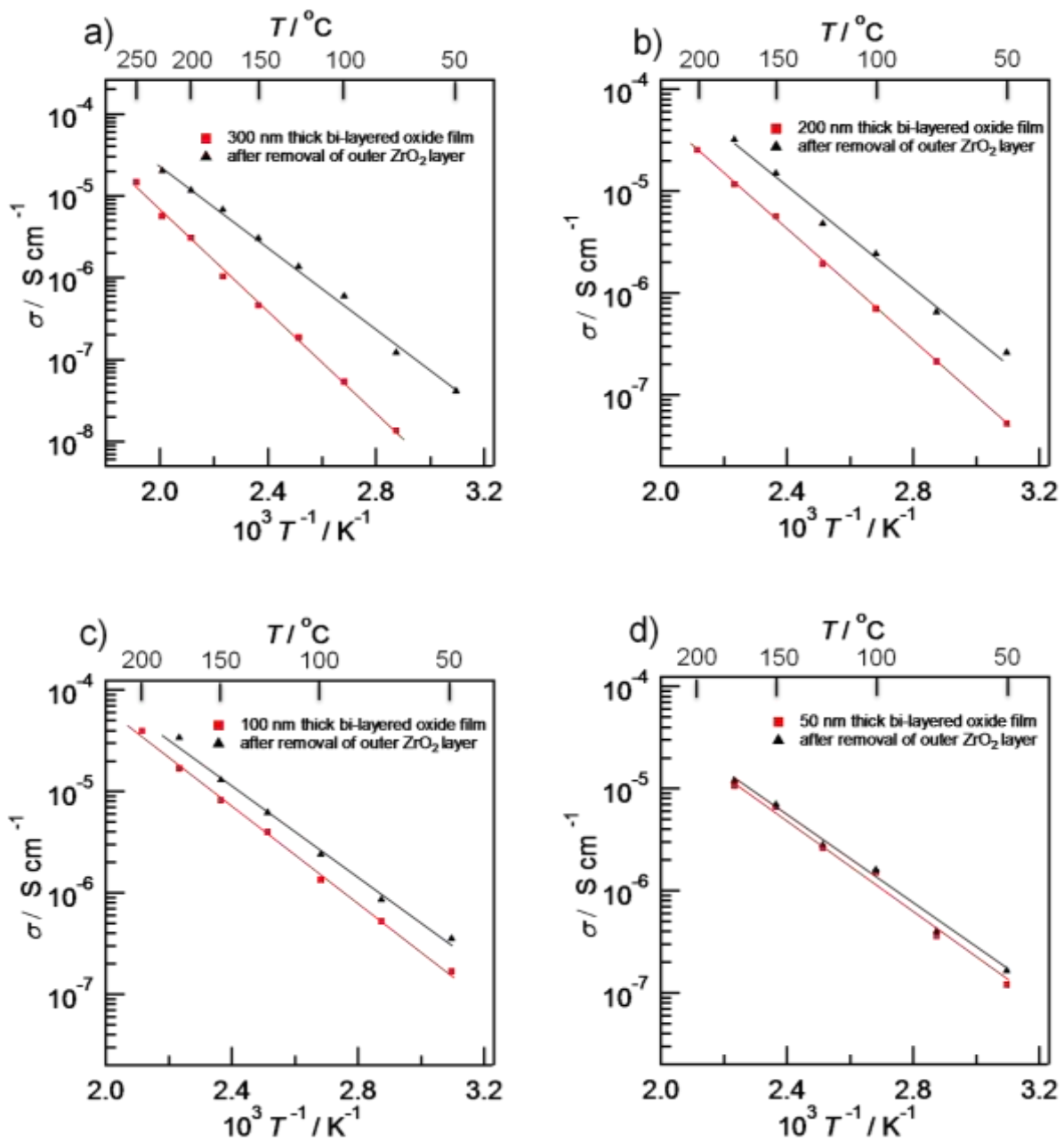


Figure 5.

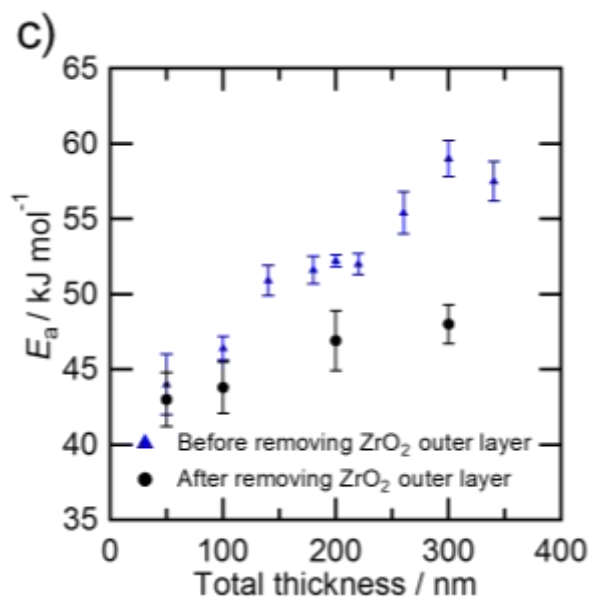
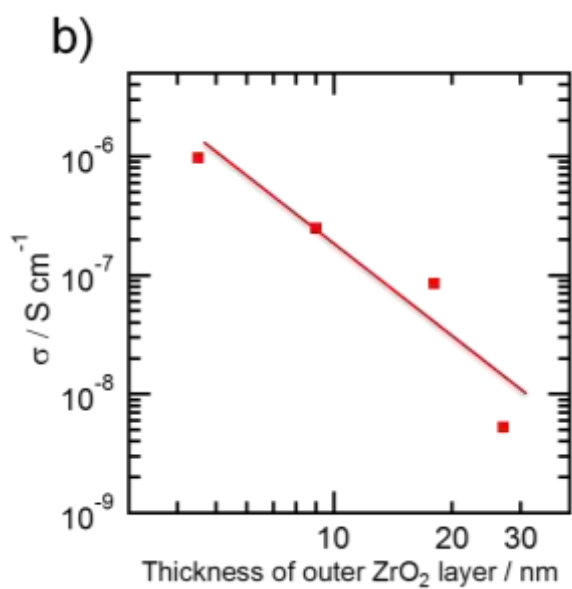
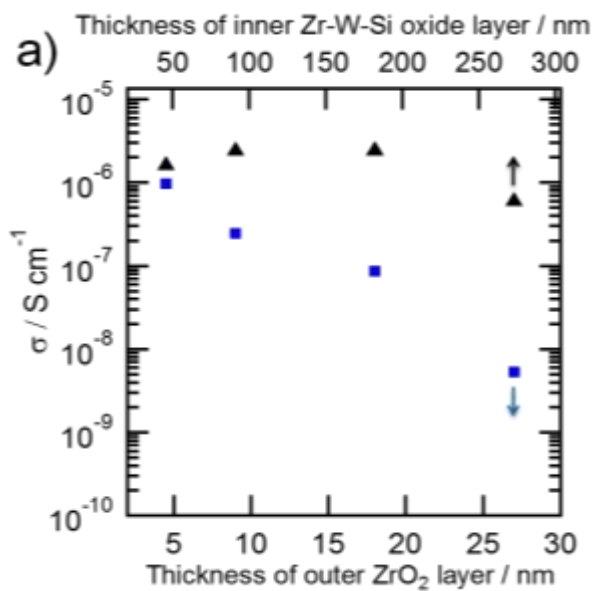


Figure 6.

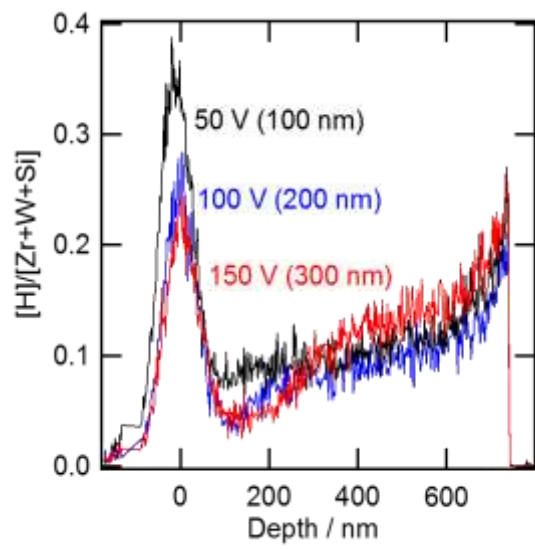


Figure 7.